

# JGR Atmospheres

## RESEARCH ARTICLE

10.1029/2019JD030882

### Key Points:

- Drizzle was observed over McMurdo at cloud  $T < -25$  degrees celsius for more than 7.5 hr in the presence of ice nucleation and growth
- Atmospheric conditions necessary for the observed drizzle are evaluated using an LES model with two-moment microphysics
- Drizzle at cloud  $T < -25$  degrees celsius may be common at the low aerosol concentrations typical of the Antarctic and the Southern Ocean atmospheres

### Supporting Information:

- Supporting Information S1
- Movie S1

### Correspondence to:

I. Silber,  
israel0silber@gmail.com

### Citation:

Silber, I., Fridlind, A. M., Verlinde, J., Ackerman, A. S., Chen, Y.-S., Bromwich, D. H., et al. (2019). Persistent Supercooled Drizzle at Temperatures below  $-25^{\circ}\text{C}$  Observed at McMurdo Station, Antarctica. *Journal of Geophysical Research: Atmospheres*, 124, 10,878–10,895. <https://doi.org/10.1029/2019JD030882>









Received 24 APR 2019

Accepted 8 SEP 2019

Accepted article online 11 SEP 2019

Published online 22 OCT 2019

## Persistent Supercooled Drizzle at Temperatures Below $-25^{\circ}\text{C}$ Observed at McMurdo Station, Antarctica

Israel Silber<sup>1</sup> , Ann M. Fridlind<sup>2</sup> , Johannes Verlinde<sup>1</sup> , Andrew S. Ackerman<sup>2</sup> , Yao-Sheng Chen<sup>3,4</sup> , David H. Bromwich<sup>5,6</sup>, Sheng-Hung Wang<sup>5</sup> , Maria Cadetdu<sup>7</sup> , and Edwin W. Eloranta<sup>8</sup> 

<sup>1</sup>Department of Meteorology and Atmospheric Science, Pennsylvania State University, University Park, PA, USA, <sup>2</sup>NASA Goddard Institute for Space Studies, New York, NY, USA, <sup>3</sup>Chemical Sciences Division, Earth System Research Laboratory, National Oceanic and Atmospheric Administration, Boulder, CO, USA, <sup>4</sup>Cooperative Institute for Research in Environmental Sciences, University of Colorado Boulder, Boulder, CO, USA, <sup>5</sup>Polar Meteorology Group, Byrd Polar and Climate Research Center, Ohio State University, Columbus, OH, USA, <sup>6</sup>Atmospheric Sciences Program, Department of Geography, Ohio State University, Columbus, OH, USA, <sup>7</sup>Argonne National Laboratory, Argonne, IL, USA, <sup>8</sup>Space Science and Engineering Center, University of Wisconsin, Madison, WI, USA

**Abstract** The rarity of reports in the literature of brief and spatially limited observations of drizzle at temperatures below  $-20^{\circ}\text{C}$  suggest that riming and other temperature-dependent cloud microphysical processes such as heterogeneous ice nucleation and ice crystal depositional growth prevent drizzle persistence in cold environments. In this study, we report on a persistent drizzle event observed by ground-based remote sensing measurements at McMurdo Station, Antarctica. The temperatures in the drizzle-producing cloud were below  $-25^{\circ}\text{C}$  and the drizzle persisted for a period exceeding 7.5 hr. Using ground-based, satellite, and reanalysis data, we conclude that drizzle was likely present in parts of a widespread cloud field, which stretched more than  $\sim 1,000$  km along the Ross Ice Shelf coast. Parameter space sensitivity tests using two-moment bulk microphysics in large eddy simulations constrained by the observations suggest that activated ice freezing nuclei and accumulation-mode aerosol number concentrations aloft during this persistent drizzle period were likely on the order of  $0.2\text{ L}^{-1}$  and  $20\text{ cm}^{-3}$ , respectively. In such constrained simulations, the drizzle moisture flux through cloud base exceeds that of ice. The simulations also indicate that drizzle can lead to the formation of multiple peaks in cloud water content profiles. This study suggests that persistent drizzle at these low temperatures may be common at the low aerosol concentrations typical of the Antarctic and Southern Ocean atmospheres.

## 1. Introduction

Drizzle at subfreezing temperatures has been detected in various studies, both in midlatitudes (e.g., Cober & Isaac, 2012; Ikeda et al., 2007; Rosenfeld et al., 2013) and the polar regions (e.g., Lawson et al., 2001; Verlinde et al., 2013). In convective clouds, it is possible that drizzle and raindrops may be lofted from the  $0^{\circ}\text{C}$  isotherm up to temperatures as low as  $-20^{\circ}\text{C}$  when the mean updrafts are  $>6\text{ m/s}$  (Carey & Rutledge, 2000; Zipser & Lutz, 1994). However, in stratiform clouds or convective clouds with weaker updrafts, the formation and persistence of drizzle may depend on the condensate supply (e.g., by adiabatic lifting) and collision coalescence rate,  $C_i$ , exceeding the sum of heterogeneous freezing, ice crystal depositional growth, and/or riming rate,  $D_i$  (e.g., Cober et al., 1996; Ikeda et al., 2007; Lawson et al., 2001; Rosenfeld et al., 2013), that is,  $C_i > D_i$ .

Collision coalescence of cloud droplets is the predominant mode of drizzle production (e.g., Rasmussen et al., 2002), generally requiring low cloud condensation nuclei (CCN) concentrations and/or high liquid water path (LWP) for the development of sufficiently broad droplet size distributions (e.g., Comstock et al., 2004; Pruppacher & Klett, 1997, pp. 581–598). The formation of drizzle without an active collision coalescence process has also been reported when droplet number concentrations are extremely low (Mauritsen et al., 2011). Such number concentration requirements make this process more likely to be active in a maritime environment (e.g., Cober et al., 1996, 2001), or potentially, in stable environments where updrafts are very weak.

The  $C_i > D_i$  requirement suggests that the ice crystal concentrations should also be sufficiently low (hence, smaller  $D_i$ ) to enable drizzle formation and persistence (e.g., Rasmussen et al., 2002). Nonetheless, drizzle can be maintained at greater  $D_i$  if  $C_i$  is greater still. For example, while Cober et al. (1996) measured ice

crystal number concentrations of  $0.08 \text{ L}^{-1}$  in supercooled drizzle regions with weak updrafts ( $<0.1 \text{ m/s}$ ), Ikeda et al. (2007) reported ice crystal number concentrations  $<2 \text{ L}^{-1}$  in drizzle formation regions, which experienced consistent updrafts stronger than  $0.5\text{--}1 \text{ m/s}$ .

Ice crystal concentrations sufficiently low for drizzle formation can be found at temperature ranges outside the secondary ice formation region (Geresdi et al., 2005), either in a relatively pristine environment with low ice freezing nuclei (IFN) concentrations (e.g., Antarctica; Bromwich et al., 2012) or in cloud in which IFN were depleted from the drizzle formation regions (from a Lagrangian perspective) by ice precipitation (Ikeda et al., 2007; Rosenfeld et al., 2013). However, the nucleation efficiency of IFN sharply increases with decreasing temperature and/or increasing ice supersaturation (Meyers et al., 1992; Phillips et al., 2008), which steeply rises at water saturation with decreasing temperatures. Therefore, drizzle formation is expected to be rarer and of shorter duration in colder clouds. For example, Rosenfeld et al. (2013) detected drizzle at  $-21^\circ\text{C}$  along a flight track of 53 km, whereas Lawson et al. (2001) reported a smaller 10-km drizzle pocket ( $\sim 100 \text{ m}$  below cloud top) at an even lower temperature of  $-25^\circ\text{C}$ , which was completely depleted at the same location only two minutes later (and 30-m lower). The lowest temperature at which drizzle has been reported, to the best of our knowledge, is  $-28^\circ\text{C}$ , observed by Korolev et al. (2002) over a 3-min period (18-km flight track).

In this study we document the occurrence of persistent drizzle formation for over 7.5 hr in a shallow, mixed-phase cloud layer with temperatures ranging between  $-25$  and  $-29^\circ\text{C}$  (from cloud base to cloud top), which was observed using remote sensing measurements at McMurdo Station, Antarctica ( $77.85^\circ\text{S}$ ,  $166.72^\circ\text{E}$ ;  $\sim 70 \text{ m}$  above mean sea level). The measurements were gathered as part of the U.S. Department of Energy Atmospheric Radiation Measurement (ARM) Facility's (Mather & Voyles, 2013) 2016 ARM West Antarctic Radiation Experiment (AWARE) field campaign (Lubin et al., 2015; Witze, 2016). In addition, we use large eddy simulations (LES) constrained by these measurements to evaluate the conditions required for drizzle formation at these temperatures.

## 2. Drizzle Event Observations

The drizzle was detected at McMurdo Station on 16 August 2016, between 05:05 and 12:45 UTC (a total of 460 min, all at night), in a persistent mixed-phase cloud that lasted for nearly 39 hr at temperatures ranging between  $-23$  and  $-29^\circ\text{C}$ , which was first observed  $\sim 10 \text{ hr}$  prior to the period discussed in this study. A deep cyclone centered over the Southern Ocean to the north of McMurdo Station throughout the event generated northeasterly winds across the eastern Ross Sea, which advected warm and moist marine air towards the Ross Ice Shelf (RIS; Figure 1a). The cyclone-driven wind confluence with the RIS southwesterly katabatic flow resulted in convergence along the RIS coast, including around McMurdo Station (relatively weaker winds in Figure 1a; see Figure S1 in the supporting information for high-resolution flow patterns around Ross Island). Widespread enhanced top of atmosphere (TOA) upwelling longwave (LW) radiation footprints were measured in this coastal region during this event by the Clouds and the Earth's Radiant Energy System (CERES; Wielicki et al., 1996; dashed red shape in Figure 1b) instrument on National Aeronautics and Space Administration (NASA)'s Aqua satellite.

Figures 2a and 2b show the High Spectral Resolution Lidar (HSRL; Eloranta, 2005) particulate backscatter cross-section ( $\beta_p$ ) and linear depolarization ratio (LDR) measurements during the drizzling period. The liquid-bearing cloud regions are indicated by high  $\beta_p$  and low LDR (predominantly  $>5 \times 10^{-5} \text{ m}^{-1} \text{ sr}^{-1}$  and  $<0.08$ , respectively). Note that the HSRL backscattered signal is often extinct below the mixed-phase cloud layer top (marked by purple dots), which is determined by a Ka-band ARM Zenith Radar (KAZR) moderate sensitivity (MD) mode signal-to-noise ratio (SNR) threshold of  $-16 \text{ dB}$  (following the methodology in Silber, Verlinde, Eloranta, & Cadetdu, 2018). The ceilometer cloud base height (Morris, 2016) and HSRL liquid cloud base height (LCBH; see Silber, Verlinde, Eloranta, Flynn, & Flynn, 2018a; 2018b) data products, which are depicted by white and black dots, respectively, mostly display little variability near the mixed-phase layer base. The agreement between these two data products is good, with a typical difference of  $\sim 50\text{--}100 \text{ m}$  (cf. Silber, Verlinde, Eloranta, Flynn, & Flynn, 2018b). We refer hereafter to the HSRL data product when discussing the LCBH, as this cloud base height algorithm is more sensitive (relative to the ceilometer data product) to the level of condensation in this optically thin (per unit volume) mixed-phase cloud layer.

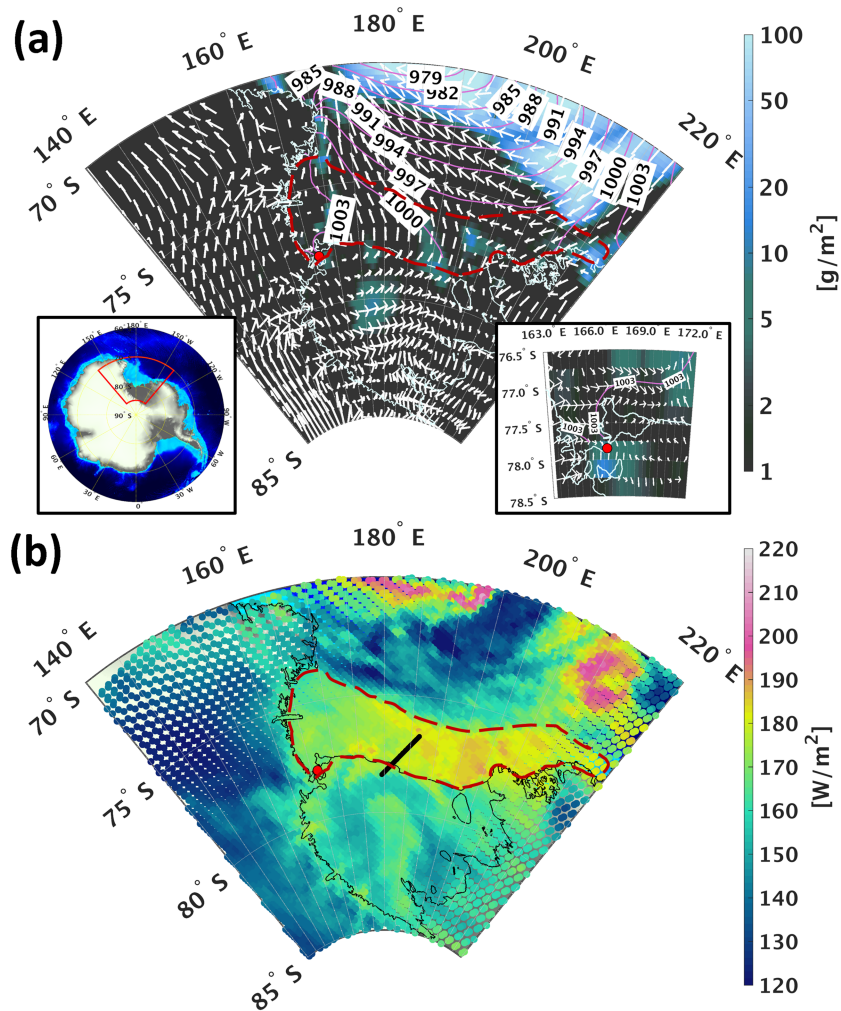


**Figure 1.** (a) Sea level pressure (in hPa; land areas are masked), integrated liquid water (cloud + rain; log-scaled color bar), and surface winds illustrated in contours, color scale, and quivers, respectively, resolved by ERA5 for 16 August 2016 at 10:00–11:00 UTC. The red circle marker designates the location of McMurdo Station (located on Ross Island). The inset panels show a topographic map of Antarctica (the red box designates the region depicted in the main panels) and a focus on the flow field surrounding Ross Island. (b) Top of atmosphere upwelling longwave radiation footprints measured by CERES Aqua on 16 August 2016, between 10:44 and 10:50 UTC. The red dashed shape highlights the region of enhanced upwelling longwave radiation discussed in the text. The thick black curve designates part of the CALIPSO satellite trajectory (10:48–10:50 UTC), in which low-level mixed-phase clouds were detected (see Figure S2 in the supporting information). The 1 arc-min topographic data were developed by the National Geophysical Data Center (NGDC, Amante, 2009) and is freely available at <https://www.ngdc.noaa.gov/mgg/global/global.html>.

Concurrent moderate  $\beta_p$  ( $\sim 10^{-5.3}$ – $10^{-4.5}$  m<sup>-1</sup> sr<sup>-1</sup>) and low LDR ( $< 0.2$ ) values are frequently observed down to  $\sim 300$  m below the LCBH (Figures 2a and 2b; see also Figures 3a and 3b), with higher LDR values closer to the surface. These higher LDR values indicate precipitating ice. The low LDR values just below the LCBH suggest that the backscattered lidar signal from these air volumes is dominated by nearly spherical scatterers, for example, falling drizzle drops (diameter  $< 0.5$  mm per Pruppacher & Beard, 1970). While specular reflection by plate ice crystals may induce similar low LDR values (see Appendix A in Silber, Verlinde, Eloranta, Flynn, & Flynn, 2018b), the cloud layer temperatures ( $T$ ; Figure 3h, left panel) were well below the plate crystal growth regime (Bailey & Hallett, 2009). Aerosol particles and cloud droplets may also produce low LDR, but the measured  $\beta_p$  values are too high and low for aerosol particles and cloud droplets, respectively (e.g., Silber, Verlinde, Eloranta, & Cadetdu, 2018, Figure 2). Moreover, the temporal variability of these  $\beta_p$ -LDR features is significantly patchier than that of a typical liquid-bearing cloud layer.



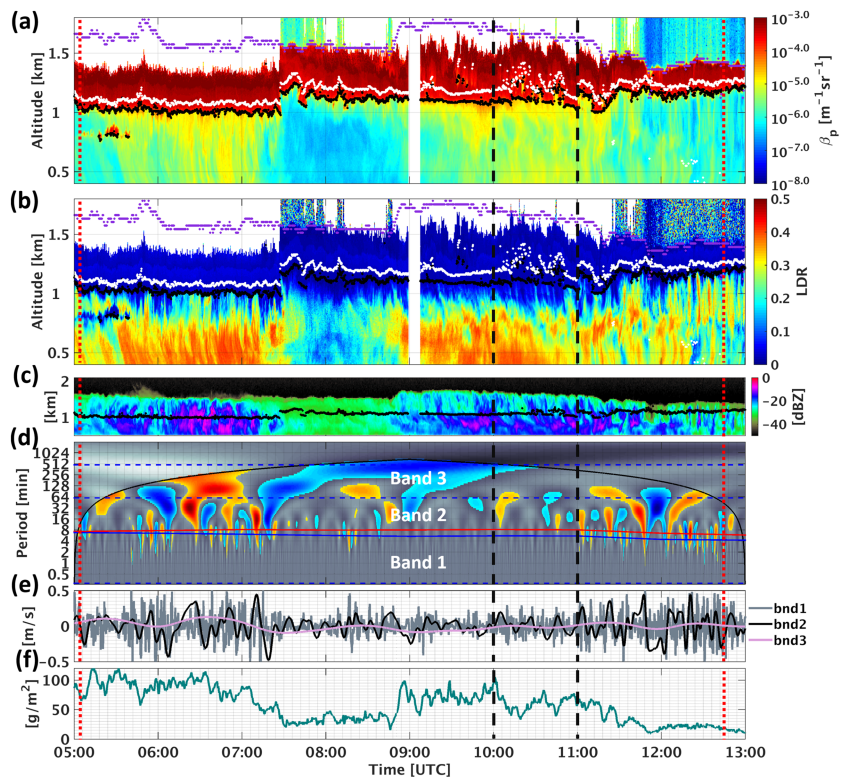


**Figure 2.** (a) High Spectral Resolution Lidar (HSRL) particulate backscatter cross section ( $\beta_p$ ; color bar in log scale). The white and black dots show the ceilometer cloud and HSRL liquid cloud base height (LCBH) data product outputs, respectively. Purple dots indicate the cloud-top height (CTH) determined using the Ka-band ARM Zenith Radar (KAZR) moderate sensitivity (MD) mode measurements (see text for details). Note that the apparent jump in the observed liquid-bearing cloud layer at 07:27 UTC is the result of a (physical) rapid ( $\sim 1$  min)  $\sim 200$  m upward shift in the lowest LCBH. (b) HSRL linear depolarization ratio (LDR). (c) KAZR integrated reflectivity factor. The “main” HSRL LCBHs used for the wavelet analysis are designated by the black dots. (d) Wavelet analysis of the most upward Doppler velocity in the KAZR Doppler velocity spectrum with signal above the noise floor ( $V_{dmax}$ ) 100 m above the main LCBH, which provides an estimate of the vertical air motion. The colored regions denote statistically significant periodicities at the 99% level. The solid black curve represents the wavelet cone of influence. The solid red and blue curves indicate the Brunt-Vaisala frequency (BVF) and the Eulerian apparent BVF for a horizontal wavelength of 4 km, respectively, calculated for McMurdo Station based on the atmospheric parameters 0–200 m above the main LCBH using the 1.1-km AMPS model output (winds are taken at the LCBH + 100 m). The solid blue curve (apparent BVF) and the three horizontal dashed blue lines (located at 17 s, 60 min, and 8 hr) partition the spectrogram into three main bands, which can represent (from the smallest to largest time scale) the cloud-scale circulation (and inhomogeneity), gravity wave scale oscillations, and synoptic-scale air motion. (e) Temporal variability of the three bands (see legend for details). (f) Liquid water path derived from microwave radiometer measurements. The vertical dotted red lines define the beginning and ending of the drizzle event. The vertical dashed black lines indicate the edges of the period represented in Figures 1 and 3.

Therefore, we deduce that these features are indicative of drizzle drops, similar to the remote sensing signatures observed by Verlinde et al. (2013).

To further support our conclusion, we examine measurements from a single hour (10–11 UTC; Figure 3), coinciding with a radiosonde release (the only in situ measurements obtained during this drizzle event). During this hour (and a large fraction of the whole drizzle event; see Figure 2c), the KAZR reflectivity factor (Figure 3c) shows frequent fall streaks below the LCBH. These regions of higher reflectivity (e.g., 10:30 UTC and 10:52–10:55 UTC) correspond with an increase in LDR with decreasing altitude right below LCBH (Figure 3b). The concurrent reflectivity and LDR patterns suggest that these fall streaks are composed of ice particles that nucleate near (or at) cloud top (Figure 3c), which have an adequate surface area to hasten evaporation of the low LDR liquid hydrometeor population.

The most upward Doppler velocity in the KAZR Doppler velocity spectrum with signal above the noise floor,  $V_{dmax}$ , is depicted in Figure 3d.  $V_{dmax}$  can be used as an estimation of the vertical air motion in regions where



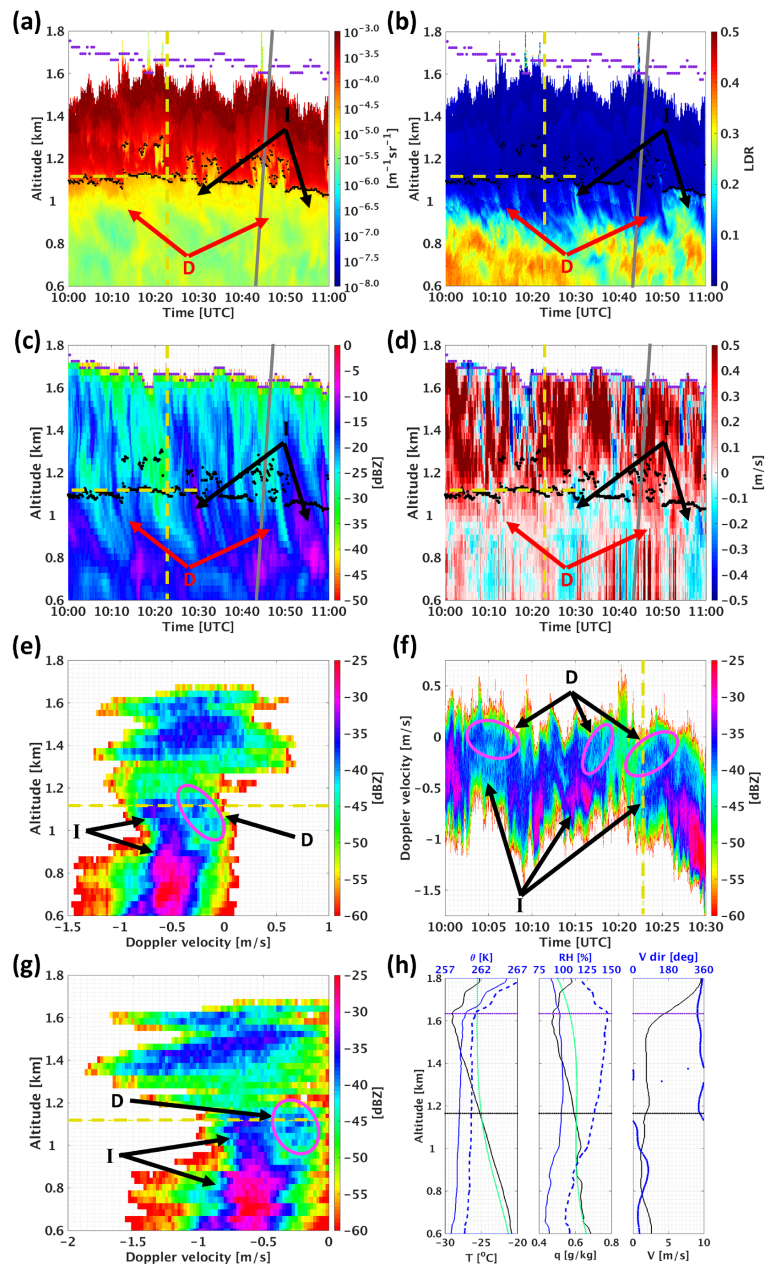


**Figure 3.** Measurements gathered during the drizzle event on 16 August 2016, between 10:00 and 11:00 UTC: (a) HSRL  $\beta_p$  (log-scaled colorbar), (b) HSRL LDR, (c) KAZR integrated reflectivity factor, (d) KAZR  $V_{dmax}$ , (e) vertical profile of the KAZR Doppler spectra at 10:22:47 UTC, (f) temporal evolution of the KAZR Doppler spectra at 1118 m altitude between 10:00–10:30 UTC, (g) same as panel (e) but with the spectra shifted by  $V_{dmax}$  to 0 m/s, (h) balloon (released at 10:41 UTC) sounding measurement profiles, where the solid black curves in the left, middle, and right panels illustrate the temperature, specific humidity ( $q$ ), and horizontal wind speed, and the solid (dashed) blue curve shows the potential temperature  $\theta$  (equivalent potential temperature  $\theta_e$ ), relative humidity with respect to water (ice), and the wind direction, respectively. The dotted green curves in the left and middle sounding panels depict the temperature and  $q$  profiles (respectively) used for the 1-D “backward” model run (see section 3). All the KAZR parameters shown in this figure are from the MD mode measurements. The gray lines illustrated in panels (a)–(d) denote the balloon time-altitude location (horizontal coordinates are different from the HSRL and KAZR field of view). The black and purple dots in panels (a)–(d) and (h) mark the HSRL liquid cloud base height and KAZR cloud-top height, respectively. The vertical (horizontal) dashed yellow lines in panels (a)–(g) designate the time (altitude and time period) of the spectra presented in panels (e) and (f). The letter “D” and its corresponding arrows and ellipses point to some of the drizzle time-height locations in the HSRL and KAZR profiles (panels a–d) and indicate the drizzle spectra signatures in panels (e)–(g) (ice crystal locations and spectra signatures are indicated by the letter “I”).

there are droplets large enough (and/or at a sufficient concentration) to produce a detectable signal and small enough to have terminal velocities that are slow relative to the air motion.  $V_{dmax}$  may be upward-biased because of turbulent broadening, which for the data above the lowest LCBH in Figure 2d is equivalent to  $\sim 0.2\text{--}0.4$  m/s (Appendix A). Suitable droplet populations can be found within mixed-phase cloud layers, although not necessarily at the LCBH where the droplet volume can be too small to produce backscattered signals above the KAZR noise floor when there is no drizzle. Verlinde et al. (2013), Figure 9) showed for a weakly drizzling case that  $V_{dmax}$  decreased slowly across the LCBH, with the evaporating small drizzle drops (diameter  $< 200$   $\mu\text{m}$ ) providing the backscatter necessary for detection by KAZR. In these drizzle-bearing air volumes below the LCBH, the liquid water content (LWC) is significantly lower than within the cloud layer, and hence, the effect of spectral broadening biases described in Appendix A are negligible. When the total volume of drizzle drops in the radar volume decreases below the KAZR detectable signal, the  $V_{dmax}$  signal comes from the faster falling ice in the volume, and hence, no longer serves as a proxy for the air motion. In regions with stronger liquid hydrometeor signals below the LCBH (Figures 3a and 3b) higher saturation ratios driven by weak updrafts of up to  $\sim 0.1$  m/s (Figure 3d) may help counter the desiccation effects of the ice. During the stronger ice showers, when liquid hydrometeors are mostly absent,  $V_{dmax}$  no longer represents the vertical air motion. Rather, the observed negative values represent the Doppler velocity of the slowest falling ice particles.

The KAZR spectra (velocity bin resolution of 2.34 cm/s) show distinct signatures of a slow falling hydrometeor population at and below the LCBH, both in the vertical spectra profiles (e.g., at  $\sim 10:22$  UTC; circled in Figure 3e) and in the temporal evolution of the spectra at a fixed elevation close to the LCBH (e.g., at 10:00–10:30 UTC; Figure 3f, circled areas). This Doppler spectra population cannot be attributed to humidified aerosols (cf. van Dierenhoven et al., 2011), the reflectivity of which would not exceed the KAZR noise floor. The fall velocity of the hydrometeors in the circled population is  $< 0.5$  m/s, typical for drizzle drops with diameters  $< 150$   $\mu\text{m}$  (Lamb & Verlinde, 2011, Figure 9.5). The small decrease in the population's fall speed relative to  $V_{dmax}$  seen with decreasing altitude (e.g., at  $\sim 10:22$  UTC; Figure 3g) is consistent with drops evaporating below the LCBH. The ice population peak fall velocity is approximately constant with decreasing height at these drizzle-bearing altitudes, implying that riming is likely not a very active process at these heights. Such a lack of a riming signature suggests insufficient LWC and/or number concentrations (e.g., Jensen & Harrington, 2015). Although individual ice crystals growing in the ice-supersaturated conditions beneath the LCBH should see a monotonic increase in fall speed along Lagrangian trajectories, such a signal is not readily evident in the instantaneous snapshot represented in the spectrograph of many such trajectories captured at various stages of evolution. A similar lack of an active riming process is indicated in the first 90 min of the drizzle event when maximum LWP was measured (Figure 2f).

The balloon sounding occurred during a period in which the HSRL drizzle signature was observed down to  $\sim 850$  m. As shown by these measurements (Figure 3h), the mixed-phase cloud layer  $T$  ranged between  $-25$  and  $-29$   $^{\circ}\text{C}$  (left panel). Beneath the LCBH, the relative humidity with respect to water ( $RH_w$ ; middle panel) declines from saturation with decreasing height. The specific humidity ( $q$ ) profile suggests that the mixed-phase cloud and the layer below it (down to  $\sim 1,000$  m) are not well mixed as not uncommonly expected in stratiform mixed-phase clouds (e.g., Fridlind et al., 2012), although the equivalent potential temperature ( $\theta_e$ ; left panel) does show a tendency for low stability ( $d\theta_e/dz \approx 0.33$  K/km on average in the altitude range of 1.0–1.6 km). Gaps in the lowest liquid cloud base intermittently reveal another cloud base that is  $\sim 100$ -m higher, suggesting that LWC does not exhibit a linear profile with a persistent vertical structure. Lack of vertical shear of the horizontal wind, as well as the weak wind speed ( $\sim 2$  m/s; right panel), also do not support consistently strong mixing.

Taken together, the observations discussed above, that is, the liquid hydrometeor desiccation by stronger ice showers below LCBH, the low Doppler fall velocities of an independent hydrometeor population, and the subsaturation  $RH_w$  below the LCBH, support our conclusion that persistent drizzle formation occurred throughout this long-lasting event.

The earlier work on drizzle formation in mixed-phase clouds suggested that updraft strength and duration may play a role (e.g., Cober et al., 1996; Ikeda et al., 2007). Because McMurdo Station is situated close to complex orography, larger-scale forcing of the vertical velocity field should be considered to understand all the factors forcing the formation of drizzle. Using the Doppler radar observations, we perform a wavelet

analysis (Torrence & Compo, 1998) of  $V_{dmax}$  100 m above the LCBH throughout the entire drizzle event, to examine whether the drizzling periods correspond with local wave activity. We assume that cloud droplets at this height within the mixed-phase layer are consistently large enough to be detected by the KAZR and small enough to represent an estimation of the vertical air motion. The bias in  $V_{dmax}$  identified in Appendix A is inherently removed in the wavelet analysis. The “main” liquid-bearing cloud base used as a reference for this analysis (depicted in Figure 2c) is identified in intermittent periods of multiple liquid-bearing layers (see Figures 2a and 2b and 3a and 3b) by examining its height consistency over time. LCBHs (at times with multiple liquid-bearing layers) that depart from the median  $\pm 2$  standard deviations (SDs) of all LCBH values between the 45th and 55th percentiles in 20-min windows (with 10 min overlap) are rejected from the analysis. This filtering step, which produced LCBH consistency, is followed by the removal of all residual multi-layer LCBHs above the lowest layer; Figures 2a and 2b show that the “main” liquid-bearing layer is predominantly the lowest one in multilayer cases. Finally, LCBH values are linearly interpolated at times where LCBHs are not detected or no HSRL data are available.

The wavelet analysis spectrogram (Figure 2d) shows statistically significant oscillations (colored patches) at different times and periods. Statistical significance is determined here by comparison of the wavelet spectrum with a red noise spectrum and utilizing a chi-squared test (Torrence & Compo, 1998) at the 99% level, following the methodology of Miles and Verlinde (2005). Note that significance tests are not performed outside the cone of influence (black solid curve in Figure 2d), as the spectral power in that region is affected by zero padding of the data necessary for the analysis procedures (see Torrence & Compo, 1998).

The spectrogram is divided into three main bands, subjectively selected to represent from the smallest to largest time scale the cloud-scale circulation and inhomogeneity, gravity wave (GW) scale oscillations, and synoptic-scale vertical air motion. The band limits (dashed and solid blue lines in Figure 2d) are located at 17 s, a variable  $\sim 4$ –7 min, 60 min, and 8 hr. The lowest period threshold was chosen to correspond with the second-highest frequency received by the wavelet analysis; hence, the fastest oscillating component, which includes the turbulent eddies, is overlooked in this analysis. The variable 4- to 7-min periodicity corresponds with the apparent Brunt-Vaisala frequency (BVF) at McMurdo Station under the assumption of a horizontal wavelength of 4 km. This apparent BVF was calculated 0–200 m above the LCBH using the Antarctic Mesoscale Prediction System (AMPS, on a 1.1-km horizontal mesh; Powers et al., 2012) model output bilinearly interpolated to McMurdo Station's coordinates. The horizontal wavelength value matches small-scale topographic features to the northwest-west and south of McMurdo Station, which may act as a source of GWs induced by orographic lifting, given the prevailing large-scale wind direction (and intensity over the McMurdo region (Figure S1 in the supporting information).

The GW band (band 2) shows frequent statistically significant oscillations, more often than the two other bands. The reconstruction of the band time series (Figures 2e; cf. Torrence & Compo, 1998) indicates that these GW oscillations can reach amplitudes of up to  $\sim 0.5$  m/s. However, the variable GW-driven air motion, in sign and strength, does not necessarily produce drizzle-favored conditions (e.g., continuous lifting), which were reported in previous supercooled drizzle case studies (e.g., Ikeda et al., 2007). This absent correlation is evident here by the fact that drizzle signatures are observed below the LCBH both during positive and negative oscillation periods (compare Figure 2e to Figure 2a and 2b), whether these oscillations are intense (e.g., 11:45–12:00 UTC) or weak (e.g., 08:30–09:30 UTC). Some influence of the GWs on the liquid water may be evident, as the cloud liquid water (Figure 2f) does seem to deplete during intense oscillations (e.g., 06:30–07:30 and 11:00–12:00 UTC). The main processes that govern the desiccation of the cloud water, that is, entrainment of drier air at cloud top, ice growth, and sedimentation from the cloud-containing layer, in-cloud collisions, or riming and subsequently faster droplet scavenging via drizzle and ice precipitation, cannot be straightforwardly determined. Nonetheless, stronger ice precipitation at the base of the mixed-phase cloud layer is observed during these periods, as evident in the high LDR and concurrent higher reflectivity in Figures 2b and 2c, respectively. Further investigation of GW impact on cloud layers is beyond the scope of this study.

The persistent supercooled drizzle formation at liquid-bearing cloud temperatures  $< -25$  °C is evident both during periods with high ( $> 100$  g/m<sup>2</sup>) and very low ( $< 25$  g/m<sup>2</sup>) LWP (Figure 2f). It is produced either with or without substantial ice nucleation and growth (e.g., 06:00–07:00 and 07:35–08:20 UTC in Figures 2a–2c, respectively) and without a clear connection to GW activity (Figure 2e). As the synoptic-scale air motion



(band 3 in Figure 2e) reaches amplitudes of up to 0.13 m/s, which are comparable to the air motion detected locally over McMurdo at the LCBH during periods of drizzle (Figure 3d), and assuming based on the flow patterns (Figure 1a) and a back trajectory (BT) analysis (Figure S2 in the supporting information) that the aerosol particle concentrations in the air masses above McMurdo Station and the RIS coast are similar, we conclude that it is plausible that drizzle formation was extensive over the region of enhanced TOA upwelling longwave along the RIS coast measured by CERES (red dashed shape in Figure 1b).

We note that widespread drizzle formation along the RIS coast is not consistent with ERA5 (Hersbach & Dee, 2016) analysis (Figure 1a). However, a comparison of the water vapor mixing ratio profile during the drizzle event between the radiosonde sounding measurements from McMurdo and the corresponding grid cell in the ERA5 reanalysis indicates that ERA5 underestimates water vapor over this region by an average of ~13% for altitudes between 0 and 2 km. This underestimation could lead to an underestimation of the horizontal and vertical extent of condensate or the generation of ice clouds instead of liquid-bearing clouds (see Silber et al., 2019). For example, the ERA5 LWP at McMurdo Station (right inset panel in Figure 1a) is ~7.5 times smaller than the value derived from the microwave radiometer (Morris, 2006) measurements at McMurdo during the same hour (10:00–11:00 UTC; Figure 2f). ERA5 does produce low amounts of liquid water along the RIS coast but does not maintain liquid water from one hour to the next at specific locations. Because there is less upwelling LW radiation at TOA in ERA5 along the RIS coast compared to CERES measurements (not shown), we argue that the enhanced upwelling radiation measured by CERES along the RIS coast indicates the occurrence of widespread, relatively tenuous, mixed-phase clouds. This interpretation is further supported by the spaceborne Cloud-Aerosol Lidar with Orthogonal Polarization (CALIOP) measurements (Winker et al., 2003) during 10:48–10:50 UTC, which provide evidence that the enhanced TOA upwelling longwave radiation along the RIS coincides with low-level mixed-phase cloud layers (red dashed shape in Figure 1b; Figure S2 in the supporting information). The variability in mixed-phase cloud heights seen in the CALIOP measurements (Figures S2a and S2b) explains the patchiness in the enhanced upwelling radiation region. While the existence of such clouds does not necessarily mean that drizzle was produced in large sectors of this widespread cloudy region, it certainly is a possibility.

### 3. Drizzle Event Modeling

A leading question that arises from these observations is how low the activated IFN and aerosol particle concentrations need to be to allow persistent drizzle formation at these low temperatures. To provide estimates for these two parameters, we use the observations described above to constrain model simulations. Our approach is meant to represent a plausible, quasi-idealized scenario under which the observed cloud formed.

For large eddy simulations, we use the Distributed Hydrodynamic Aerosol and Radiative Modeling Application (DHARMA) model (Stevens et al., 2002), which includes a dynamic Smagorinsky scheme for subgrid-scale mixing (Kirkpatrick et al., 2006). DHARMA performs comparably to other LES models in case studies of mixed-phase clouds using bulk or bin microphysics; here we use a bulk microphysics scheme that prognoses two moments of the size distributions for each of three hydrometeor species: cloud water, rain, and cloud ice. Under these conditions the rain is very light and mean raindrop sizes quite small, so we will refer to rain and drizzle interchangeably.

To avoid the complications of specifying large-scale horizontal flux divergences, we translate the LES domain with the mean wind in the cloud layer, which is elevated and decoupled from the surface (see Figures 3h and 6a). Vertical air motions within a cloud layer correspond to some combination of large-scale ascent, GW oscillations, and turbulence, with implications for the relationships between aerosol particles, droplet number concentrations, and drizzle formation. Plausible scenarios of large-scale vertical motion are first obtained from BT analysis of ERA-Interim (Dee et al., 2011) reanalysis fields using the Hybrid Single-Particle Lagrangian Integrated Trajectory model (HYSPLIT; Stein et al., 2015) over the range of the observed cloud depth during the target observation time (10–11 UTC; see Figure 3). All BTs show a period of notable ascent during the 9-hr window prior to the target observation time (Figures 4a and 4b). A series of simulations for window periods from 6 to 24 hr revealed that results at 10 UTC converge for all simulations with BT windows exceeding 9 hr. The LES applies the evolving profile of large-scale vertical motions from the 9-hr back trajectories as source terms for prognostic variables computed from first-order

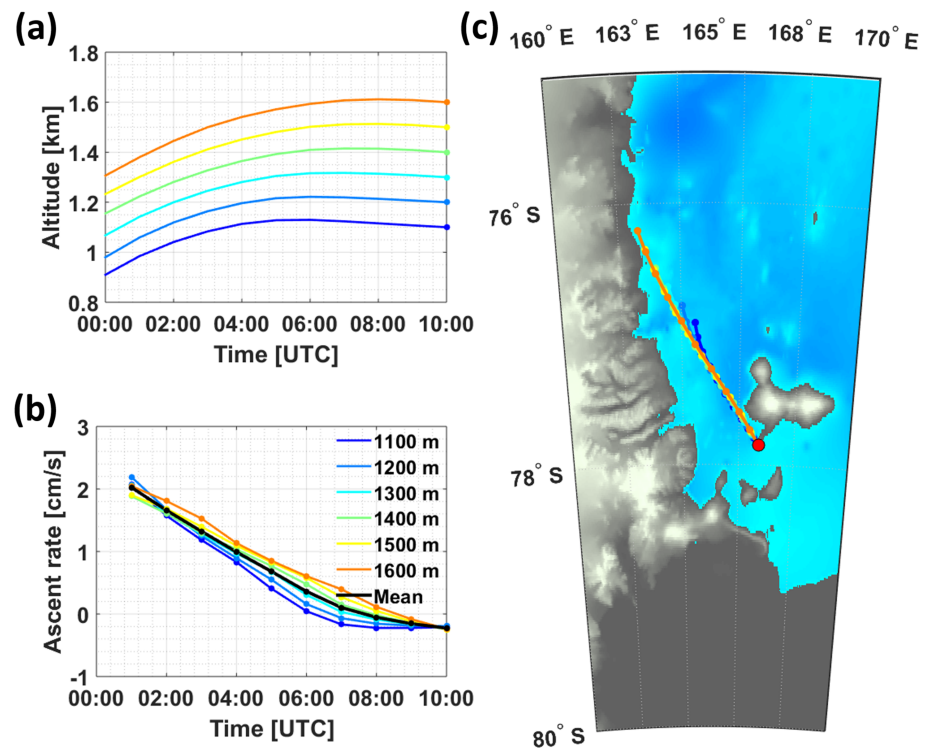


**Figure 4.** Ten-hour back trajectories and 9-hr mean ascent rates of air parcels at cloud layer heights (following the observations shown in Figure 3; see legend in panel (b)), based on the HYSPLIT model initialized with ERA-Interim reanalysis data (see text for details). The air parcel altitude, hourly ascent rates, and coordinates are shown in panels (a), (b), and (c), respectively. The red circle marker in panel (c) designates the location of McMurdo Station.

upwinding (cf. Ackerman et al., 2009) rather than including as part of the flow, which would implicate mass continuity issues.

To derive a plausible initial sounding for the LES, we apply the reversed mean BT ascent rates (i.e., an effective descent) in a DHARMA 1-D configuration for a 9-hr run, initialized with the 10:41 UTC radiosonde  $T$  and  $q$  profiles, in some resemblance to the approach taken by Field et al. (2012). The observed profiles are smoothed with spline fits using a smoothing parameter of  $10^{-6}$ , with fitting points selected to also remove the cloud signatures and produce a supersaturated layer (see the green curves in Figure 3h). The removal of the cloud signatures from the atmospheric profiles prior to the 1-D backward run allows us to examine, using the LES, the cloud formation in an elevated, stable, subsaturated moisture layer via radiative and/or large-scale ascent driven cooling. This approach is motivated by the work of Simpfendorfer et al. (2019), who showed that cloud processes themselves contribute to the characteristics of observed sounding. The objective here is to allow the LES to form and develop the cloud-induced mixed layer, as well as the cloud-top temperature and moisture inversions. The backward 1-D run accounts only for condensational adjustments with respect to liquid water. Radiative heating is ignored. At the end of this 9-hr “backward” run, no cloud water remains in the atmospheric profile, consistent with a “precloud” environment. The resulting  $T$  and  $q$  profiles, along with uniform  $\sim 2$ -m/s horizontal winds are used to initialize the LES (data are given in Table S1 and illustrated in Figure S3 in the supporting information). The LES setup and physics options are described in more detail in Appendix B. It should be noted that the results presented below are not sensitive to halving the grid spacing, doubling the domain size, reducing the time step duration, nudging to a vertically uniform 0-m/s horizontal wind, or incorporating vertical shear of the horizontal wind, from 2 m/s at 1.5 km to 9 m/s at 2 km, matching the observations in Figure 3h.

Hourly evolution of an LES run for activated IFN number concentrations ( $N_{\text{IFN}}$ ) of  $0.2 \text{ L}^{-1}$  and accumulation-mode aerosol particle concentrations ( $N_A$ ) of  $20 \text{ cm}^{-3}$  is depicted in Figure 5 (an animation file with 1-min temporal resolution is provided in the supporting information). Nonnegligible amounts of cloud

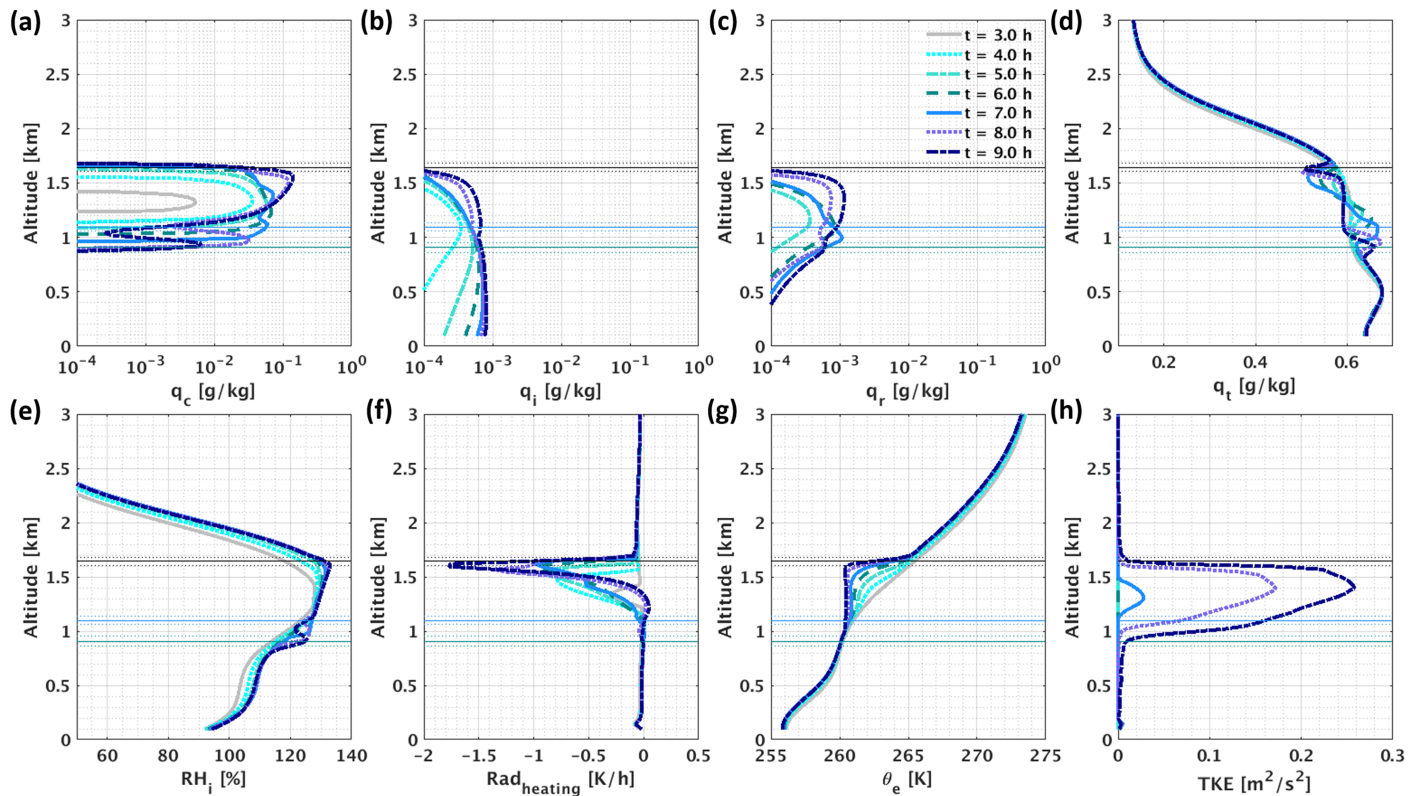


**Figure 5.** Domain-average profiles of DHARMA model output at different times (see legend) for ice freezing nuclei and accumulation-mode aerosol particle number concentrations of  $0.2 \text{ L}^{-1}$  and  $20 \text{ cm}^{-3}$ , respectively. (a–d) Mass mixing ratios of cloud water ( $q_c$ ), cloud ice ( $q_i$ ), rain ( $q_r$ ), and total water ( $q_t$ ), respectively, (e) relative humidity with respect to ice ( $RH_i$ ), (f) radiative heating rate, (g)  $\theta_e$ , and (h) turbulent kinetic energy. The solid (dotted) horizontal black, blue, and green lines represent the observed 10:00–11:00 UTC hourly mean (mean  $\pm$  standard deviation) CTH, LCBH, and drizzle base height, respectively.

water mass mixing ratio ( $q_c$ ) are first observed after 2.75 hr (Figure 5a). The cloud-top height (CTH) increases by  $\sim 360 \text{ m}$  from the cloud layer's formation until the end of the simulation. About  $100 \text{ m}$  of this CTH increase is attributable to vertical displacement of the profile forced by the large-scale ascent, while the rest of the CTH increase is associated with cooling of the overlying air by adiabatic expansion and LW radiative cooling, and weak cloud deepening through entrainment (cf. Randall, 1984) after the cloud becomes turbulent (Figure 5h).

Ice and drizzle first appear 20 min and 1.5 hr after the initial cloud formation, respectively (Figures 5b and 5c), and their downward transport via sedimentation acts to reduce the total water mass mixing ratio ( $q_t$ ) from their formation region near cloud top (Figure 5d). However, while the ice reaches the surface as a result of the supersaturated relative humidity with respect to ice ( $RH_i$ ) nearly down to the surface (Figure 5e), the drizzle evaporates below the LCBH. The net effect of the drizzle is to transport moisture from cloud top to just below the LCBH, resulting in a local maximum  $q_t$  underneath the cloud, and a negative  $q_t$  gradient over the depth of the cloud layer (Figure 5d).

At  $\sim 6.5 \text{ hr}$ , the radiative cooling near cloud-top is unable to overcome the stability there. However, because the cloud is semiopaque in the LW, radiative cooling occurs throughout the depth of the cloud layer (Figure 5f), thereby promoting enough instability in midcloud (Figure 5g) to initiate turbulent mixing (Figure 5h). This turbulent mixing, while growing in magnitude and vertically, acts to reduce the negative- $q_t$  and positive- $\theta_e$  gradients, as evident in Figures 5d and 5g. This diminution of vertical gradients leads to greater  $q_c$  near cloud top (Figure 5a), at the top of the turbulent layer (Figure 5h), and a decrease at the base of the turbulent layer (Figures 5a and 5h), by transporting warm, moist air upwards and cool, dry air downward. The higher  $q_c$  near cloud top increases the LW opacity there, which enhances cloud-top radiative cooling (Figure 5f). The enhanced radiative cooling, in turn, overcomes the stability in the upper layer of the



cloud, allowing positive feedback to develop between stronger turbulence, increasing  $q_c$  at cloud top, and cloud-top radiative cooling (Figures 5a, 5f, and 5h).

At the same time, the  $q_c$  reduction at the base of the turbulent layer just above the LCBH (Figure 5h) splits the cloud layer in the sense that a double-peaked cloud structure develops (Figure 5a). The double-peaked structure is maintained for nearly 2 hr until the end of the simulation, though it does not persist much beyond that in longer simulations (not shown). The upper  $q_c$  peak is supported by the ample cloud-top radiative cooling that invigorates the turbulence below, while the evaporation of the lower  $q_c$  peak is hindered by the local drizzle-driven  $q_t$  maximum (Figure 5d). We thus speculate that drizzle evaporating in quiescent air may play a key role in the redistribution of moisture necessary to support the formation and persistence of multi-peaked cloud water content profiles, which are occasionally observed both over Antarctica (e.g., Silber, Verlinde, Eloranta, Flynn, & Flynn, 2018b, Figure 1) and the Arctic (e.g., Silber, Verlinde, Eloranta, Flynn, & Flynn, 2018b, Figure S2; Verlinde et al., 2013, Figures 1 and 8).

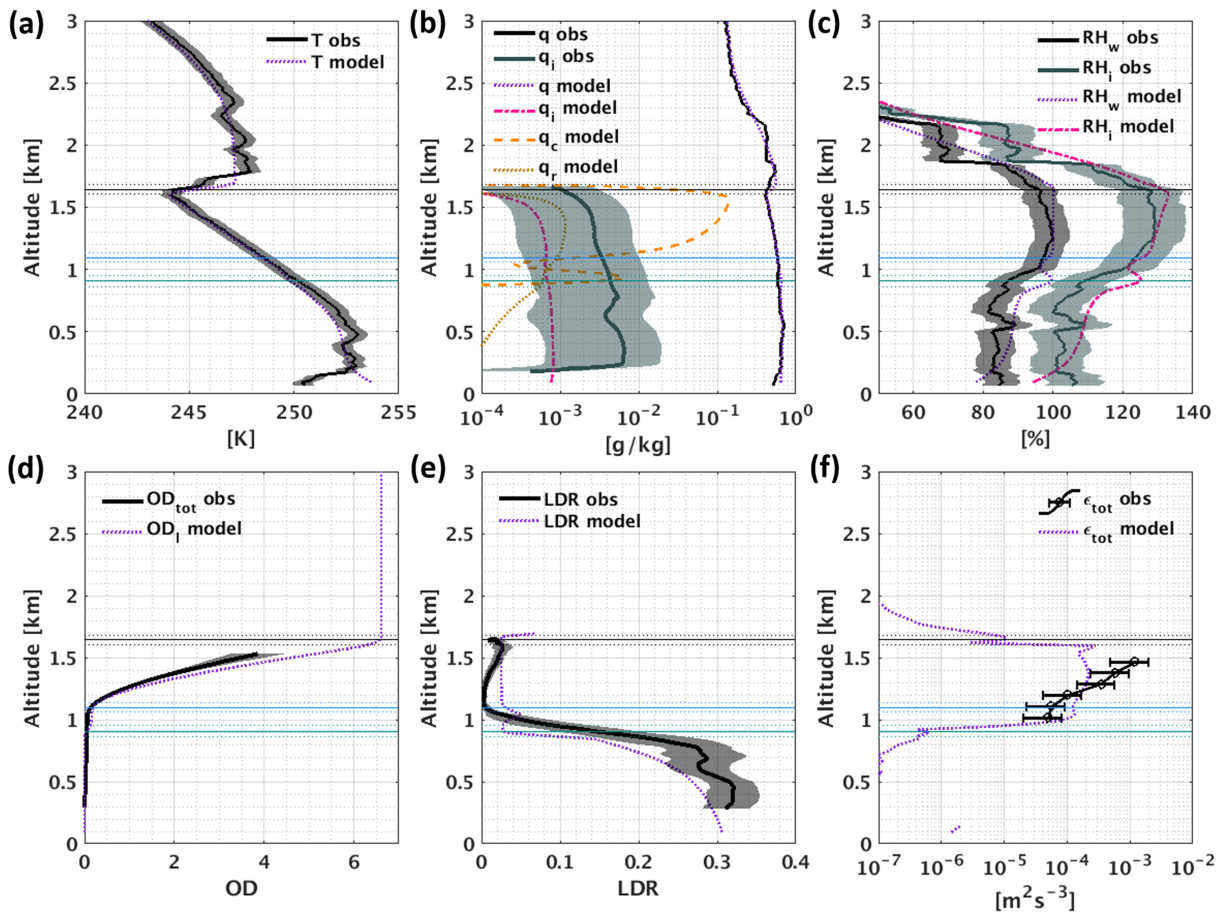
After its first appearance in the baseline model run, drizzle is continuously formed (Figure 5c), regardless of the ascent rates (Figure 4b). Drizzle is also produced in additional LES sensitivity tests, in which the same  $N_{IFN}$  and  $N_A$  values are used while the ascent rates are set to 0 cm/s from different times of the model run, before and after the initial cloud formation, until the end of these 9-hr runs (Figure S4 in the supporting information). However, the initial appearance of drizzle is delayed by up to several hours in these sensitivity tests (not shown). When the model is initialized with higher  $N_{IFN}$  and/or  $N_A$  values, drizzle production is inhibited (Figure S5), especially without continuous ascent (Figures S4). Therefore, we postulate that while low  $N_{IFN}$  and  $N_A$  are required for highly supercooled drizzle production (cf. Comstock et al., 2004; Hobbs & Rangno, 1998; Verlinde et al., 2013), large-scale ascent may hasten and potentially increase the probability for the appearance of drizzle (e.g., Ikeda et al., 2007) but is not necessary for drizzle formation.

Figure 6 illustrates the LES output for the baseline model run at 9 hr, compared with some of the observed parameters (see Appendix C for a description of the depicted parameter calculations). The model shows good agreement in the temperature (Figure 6a),  $q$  and the ice mass mixing ratio ( $q_i$ ; Figure 6b), and  $RH_w$  and relative humidity with respect to ice ( $RH_i$ ; Figure 6c). The simulated cloud top as determined by the highest altitude of nonnegligible  $q_c$  (Figure 6b) is also in good agreement with the observed CTH.

The contribution of turbulence, represented in Figure 6f by the total dissipation rate ( $\epsilon_{tot}$ ) that includes the contribution from numerics (see Chen et al., 2018), to the sharp temperature inversion just above cloud top (equivalent to the observed inversion; Figure 6a) was examined in other LES runs. These model runs in which turbulence did not develop (those with  $N_A$  of  $10 \text{ cm}^{-3}$ , see Figure S5 in the supporting information) or was prevented from developing (1-D runs; not shown) showed generally weaker inversions.

Examination of the drizzle and ice sedimentation fluxes at 1,100 m, corresponding with the mean observed LCBH and the base of the main layer in the model, indicates that moisture removal from the cloud layer via hydrometeor sedimentation is dominated by drizzle (Figure S6). However, in the model runs where  $N_A$  and/or  $N_{IFN}$  are higher by a factor of 5, moisture sedimentation flux from the cloud layer is dominated by ice as a result of the limited  $q_r$  (see Figures S5 and S6). In these simulations, the lesser  $q_r$  relative to  $q_i$  also yields greater LDR below the LCBH (calculation description provided in Appendix C), which does not correspond as well with the observed profile as the model run results presented in Figure 6e.

Finally, the simulated cumulative optical depth (OD) profile shows some overestimation within the cloud boundaries (Figure 6d), although the total cloud OD in the model is in agreement with an estimation of its true value in the observed case (see Figure S6c in the supporting information). In additional simulations initialized with a lower  $N_A$ , the cloud cumulative OD profile has a better agreement with the observations, because of the lower droplet number concentration. However, in these very small  $N_A$  simulations, the cloud-top radiative cooling is significantly reduced relative to the baseline simulation by lower LWP and cloud droplet number concentration (Figure S5; cf. Garrett & Zhao, 2006; Lubin & Vogelmann, 2006). Weaker cloud-top radiative cooling reduces turbulence production within the cloud layer, which is reflected in smaller  $\epsilon_{tot}$  and a different cloud structure (e.g.,  $q_c$  distribution), all of which show poorer agreement with the observations (see Figure S5 in the supporting information).



**Figure 6.** Observed and DHARMA model output domain-average profiles (model initialized using ice freezing nuclei and accumulation-mode aerosol particle number concentrations of  $0.2 \text{ L}^{-1}$  and  $20 \text{ cm}^{-3}$ ). (a) Temperature, (b)  $q$ ,  $q_i$ ,  $q_c$ , and  $q_r$ , (c) relative humidity with respect to water ( $RH_w$ ) and  $RH_i$ , (d) cumulative particulate and liquid water optical depths ( $OD_{\text{tot}}$  and  $OD_i$ , respectively), (e) LDR, and (f) total dissipation rate ( $\epsilon_{\text{tot}}$ ). The shaded areas (panels a–e) and error bars (panel f) designate the observation uncertainty. The solid and dotted horizontal lines are the same in Figure 5. The faint HSRL signal near the CTH allows the derivation of the LDR (with high uncertainty) but not the calculation of the  $OD_{\text{tot}}$ . For a description of the observational parameter retrievals and the modeled LDR calculation see Appendix C.

Our results suggest that both  $N_{\text{IFN}}$  and  $N_A$  were likely limited to a range of rather small values. CCN number concentration measurements at the surface obtained at McMurdo Station during the drizzle event using a CCN counter (Uin, 2016) show mean and SD values that range from  $8 \pm 3 \text{ cm}^{-3}$  at a supersaturation of 0.1% to  $89 \pm 22 \text{ cm}^{-3}$  at 1%, respectively. However, direct conclusions regarding  $N_A$  aloft cannot be made in this drizzling event because the cloud layer is decoupled from the surface (Figure 6a), and thus, aerosol concentration aloft is not linked to that at the surface (cf. Bromwich et al., 2012). With the absence of aerosol concentration measurements aloft, and based on the model comparison with the observations, we suggest that the activated  $N_{\text{IFN}}$  and  $N_A$  values during the drizzle event should have been on the order of  $0.2 \text{ L}^{-1}$  and  $20 \text{ cm}^{-3}$ , respectively. These values are within the typical range of McMurdo wintertime  $N_{\text{IFN}}$  (below  $-20^\circ \text{C}$ ) and  $N_A$  from surface-based reports (Belosi et al., 2014; Liu et al., 2018). It is important to note that these number concentrations are rough estimates, because of numerous unexplored degrees of freedom in the model configuration as well as the many uncertainties associated with the comparison of the model results with the observations. Nonetheless, the use of plausible environmental conditions and parameter values yields model results generally consistent with available observations.

#### 4. Summary and Conclusions

A persistent drizzle formation event at temperatures below  $-25^\circ \text{C}$  was detected over McMurdo Station, Antarctica. From the Eulerian perspective of the observations, we showed that the supercooled drizzle

may form at various LWP values and ice nucleation and growth rates. Large-scale ascent of tens of centimeters per second may augment the drizzle formation, but short-term (with periodicities <60 min) gravity wave activity with the same or higher amplitudes does not show any apparent influence. This observational analysis shows that the 16 August 2016 drizzle formation event was possibly widespread along the Ross Ice Shelf coast.

Using large eddy simulations, we demonstrated that persistent drizzle may form at these low temperatures regardless of the large-scale ascent magnitude, provided that the conditions are conducive to the formation of a sufficiently thick stratiform cloud layer, as long as the activated IFN and aerosol particle concentrations are sufficiently low. Under these relatively low aerosol concentration conditions, drizzle may comprise a substantial moisture sink from a highly supercooled cloud layer, consistent with Mauritsen et al. (2011), and may be associated with the formation of multiple peaks in cloud water content profiles.

Persistent ascent that may hasten and/or increase the probability for drizzle formation is plausible in the orographically forced atmosphere around the Antarctic coasts and above the inner continent (e.g., Parish & Bromwich, 1991; van den Broeke & van Lipzig, 2003). Atmospheric temperatures below  $-25^{\circ}\text{C}$  and above the homogeneous freezing temperature regime are likely to occur near the coasts and inner continent around winter and summer months, respectively (e.g., Figure 7 in Comiso, 2000), while sufficiently low aerosol concentrations are possible year-round, mainly in the inner continent (e.g., Belosi et al., 2014; Bromwich et al., 2012; Shaw, 1988). Therefore, we posit that the necessary conditions for drizzle formation at these low temperatures (based on the observational and model analyses) can be met in the Antarctic continent. Moreover, these necessary conditions are likely to occur over the Southern Ocean as well, particularly during austral winter; Zhang et al. (2010) reported on the mixed-phase cloud temperatures below  $-25^{\circ}\text{C}$ , while several studies documented low IFN and accumulation-mode aerosol concentrations (e.g., DeMott et al., 2018; Gras, 1995; Gras & Keywood, 2017; Schmale et al., 2019). While the literature lacks any reports of persistent drizzle formation at such low temperatures, we suggest that these persistent supercooled drizzle formation events may be rather common in Antarctica and the Southern Ocean. The spatial extent, climate model representation, and the potential impact of these events on the surface (e.g., radiative impact; see Mauritsen et al., 2011) are subjects for future research.

### Appendix A: Estimate of Air Motion Bias in $V_{d\max}$

The effect of turbulent air motion is to broaden the fall spectrum of droplets within the radar volume (e.g., Doviak & Zrnić, 1993, Eq. 5.67; Gossard, 1988).  $V_{d\max}$  in the measured Doppler spectrum is where this broadened spectrum disappears into the spectrum noise floor (e.g., Rambukkange et al., 2011; Shupe et al., 2008). The offset of the spectrum edge from the actual fall speed of the drops depends not only on the turbulence but also on the radar operating characteristics that determine the radar volume, the radar minimum detectable signal, and the droplet population (e.g., Shupe et al., 2008).

We calculate the mean bias for the KAZR general (GE) mode data at 1,200 m, 10–11 UTC (within the cloud layer; see Figure 3). The GE mode data are necessary for this calculation because of its sufficiently short radar pulse width. The  $\epsilon_{\text{tot}}$  values used for the calculation correspond with estimations following section 4.1 in Chen et al. (2018), but with a smaller Gaussian filter width of 500 m, to account for the shorter time series.

The Doppler spectra are simulated using the forward model described in Appendix A in Chen et al. (2018), with the radar configurations taken from the KAZR deployed at McMurdo Station. For simplicity, we assume a monodispersed cloud droplet population, with LWC and droplet number concentration ( $N_d$ ) estimates from the DHARMA simulations. For the dynamical broadening mechanisms, we only consider turbulent broadening and the beam width effect, with shear broadening neglected. The hydrometeor fall speed and vertical velocity are overlooked because we are only interested in the offset. The Doppler spectrum noise level ( $-94.6\text{ dBm}$ ) for the 1,200-m range gate is taken from the observed spectra, and background wind speed of 2 m/s is used based on the sounding measurements (Figure 3h).

We simulated 1,000 realizations for each combination of the  $\epsilon_{\text{tot}}$ , LWC, and number concentration of the cloud droplets to estimate the first Doppler spectral bin with reflectivity above the noise floor (Figure A1, top panels). An increase in the LWC and droplet diameters raises the offset by lifting the spectrum above the noise, whereas an increase in the dissipation rate broadens the spectrum, but lowers the SNR values. The mean offset values estimated varied from 0.05 m/s for low LWC ( $0.05\text{ g/m}^3$ ) cases to over 0.3 m/s for



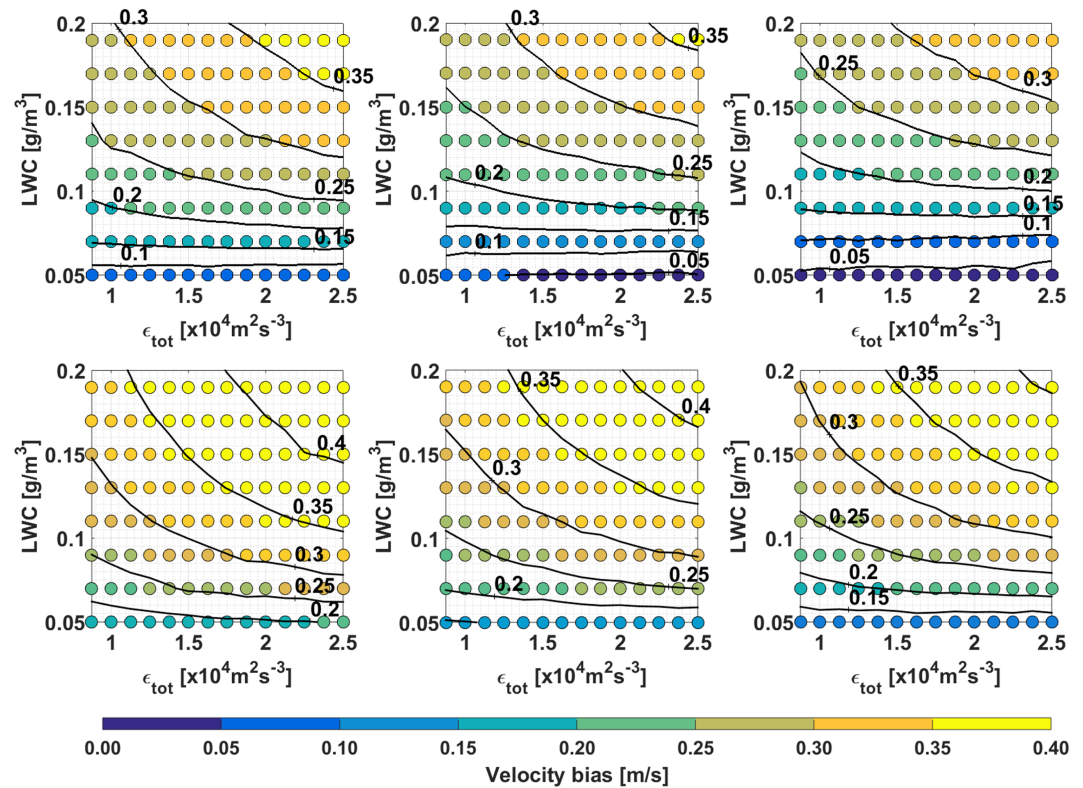


**Figure A1.** Mean bias (in m/s) of the true air velocity represented in the KAZR general (GE) mode  $V_{dmax}$  for this case (top). The panels represent (from left to right) increasing droplet number concentration (15, 20, and 25  $\text{cm}^{-3}$ , respectively). Each circle marker represents the mean bias for one set of 1,000 simulations, and the contours are isopleths of offset to indicate the dependencies. The bottom panels show the results after using the noise level in KAZR MD mode.

LWC values of 0.2  $\text{g/m}^3$ , much larger than the 0.03 m/s reported by Shupe et al. (2008) for dynamical broadening. The calculated mean offset for the GE mode is approximately 0.1 m/s (for the DHARMA output parameters in the baseline run depicted in Figure 6), close to the observed 0.08 m/s GE mode mean  $V_{dmax}$  for the 1,200-m range gate. We did not perform the full calculation for the higher sensitivity MD mode shown in Figure 3 because of the complexity in defining the radar volume, but we did simulate the impact of the lower noise level in that mode (−98.4 dBm at 1,200 m). The offset values based on the calculations with this noise level ranges (for the DHARMA output parameters) between ~0.2 and 0.3 m/s (Figure A1, bottom panels), which corresponds with the mean  $V_{dmax}$  value of 0.27 m/s at 1,200 m in the MD measurements between 10 and 11 UTC.

## Appendix B: DHARMA Model Setup

The following setup and physics options are used in DHARMA. A computational domain size of 3 km ( $x$  axis)  $\times$  3 km ( $y$  axis)  $\times$  10 km ( $z$  axis) is used with a 50-m horizontal and 25-m vertical mesh between 500 and 2,000 m, linearly stretched above and below. At each time step, the large-scale vertical motion profile is set to a uniform value between 100 and 3,000 m and interpolated linearly to zero at the surface below and at 4,000-m aloft, where the uniform values are taken as the linearly interpolated mean BT ascent rates (black curve in Figure 4b). Dynamics are integrated with a maximum time step of 5 s, reduced when required to prevent the advective Courant-Friedrichs-Lewy number from exceeding 0.8. Microphysics is treated following the Morrison et al. (2009) two-moment scheme with cloud water, rain, and cloud ice (no snow or dense ice class), with a prognostic saturation excess following Morrison and Grabowski (2008). The relative dispersion of the cloud drop size distribution is fixed at 0.3 per Geoffrey et al. (2010). Diurnal radiative transfer is computed column-wise every 60 s in 44 wavelength bins using a two-stream model (Toon et al., 1989) with water vapor continuum absorption (Clough et al., 1989). The temperature and water vapor of the model

overlying the LES model domain, which control the downwelling longwave flux at the domain top, are adjusted to match fluxes derived from observations. Liquid particle scattering and absorption coefficients are computed from the Lorenz-Mie theory (Toon & Ackerman, 1981). Ice particle scattering and absorption coefficients account for nonsphericity using the approach described by van Diedenhoven et al. (2012). Surface skin temperature is fixed at 250 K, and surface turbulent fluxes are fixed to zero.

For simplicity, we specify a monomodal lognormal aerosol particle size distribution with a geometric mean radius of 0.1  $\mu\text{m}$  and geometric SD of 2, approximated from surface measurements during AWARE (Liu et al., 2018). Aerosol activation follows Abdul-Razzak and Ghan (2000), in which the supersaturation is taken as the local minimum during a time step using the semianalytic treatment of Morrison and Grabowski (2008), which neglects activation (cf. Vogelmann et al., 2015). Ice initiation is limited to idealized immersion-mode freezing using the approach described by Ovchinnikov et al. (2014), wherein cloud ice crystals are introduced wherever a grid cell is liquid-saturated and the ice number concentration is below the specified value, referred to as  $N_{\text{IFN}}$ . This approach leaves two variable parameters: the number concentrations of the aerosol particle size distribution ( $N_A$ ) and the threshold in-cloud ice number concentration below which additional ice will be initiated ( $N_{\text{IFN}}$ ).

## Appendix C: Retrieval of the Observational Parameters and Modeled LDR

The 10:41 UTC radiosonde measurements are used as the temperature and  $\text{RH}_w$  profiles. Measurement uncertainty values are taken from Holdridge et al. (2011).  $q$  and  $\text{RH}_i$  are calculated using the formulation in Murphy and Koop (2005).

The  $q_i$  is calculated by dividing the IWC estimates by the dry air density (calculated based on the sounding measurements). The IWC is estimated from the radar reflectivity and the temperature profile following Hogan et al. (2006). The  $q_i$  uncertainty is taken from the potential bias in the methodology as shown in Heymsfield et al. (2008, their Figures 9–15).

The dissipation rate  $\epsilon_{\text{tot}}$  is calculated between 1,020 and 1,470 m in 90-m intervals using the KAZR's GE mode data, following the methodology of Chen et al. (2018).  $\epsilon_{\text{tot}}$  is not calculated for higher altitudes, because continuous KAZR records are necessary, and the GE mode data are rather patchy closer to cloud top. The  $\epsilon_{\text{tot}}$  calculations are performed over the longest continuous KAZR record in each altitude between 10 and 11 UTC, using a Gaussian filter width of 0.5 km. The  $\epsilon_{\text{tot}}$  uncertainty is estimated to be 60%, based on the  $\epsilon_{\text{tot}}$  sensitivity to the width of the Gaussian filter (see Chen et al., 2018).

The observed drizzle base altitude is determined 7.5 m (one HSRL range gate) above the highest HSRL range gate where  $\beta_p < 10^{-5.3} \text{ m}^{-1} \text{ sr}^{-1}$  and the  $\text{LDR} \geq 0.2$ . These  $\beta_p$  and LDR threshold values were determined after careful examination of the HSRL parameters together with the KAZR spectra throughout the drizzle event. The values of the observed drizzle base altitude, LCBH, CTH, particulate optical depth ( $\text{OD}_{\text{tot}}$ ; taken from the HSRL measurements), and LDR, and their uncertainties (all illustrated in Figure 6) are taken as the 10–11 UTC hourly mean and SD, respectively.

The model LDR is calculated at each altitude level by weighting the typical LDR values for liquid and ice by the horizontal domain's mean projected area per unit volume of liquid (droplets + rain) and ice hydrometeors, respectively (a hydrometeor population's projected area is excluded when its mass mixing ratio is smaller than  $10^{-3} \text{ g/km}$ ). The typical LDR values for liquid (0.025) and ice (0.32) are chosen as the LDR value of these hydrometeor population peaks in a 2-D  $\beta_p$  versus LDR histogram (e.g., Figure 2 in Silber, Verlinde, Eloranta, & Cadeddu, 2018), based on the 10–11 UTC hourly data.

## References

- Abdul-Razzak, H., & Ghan, S. J. (2000). A parameterization of aerosol activation: 2. Multiple aerosol types. *Journal of Geophysical Research*, 105(D5), 6837–6844. <https://doi.org/10.1029/1999JD901161>
- Ackerman, A. S., vanZanten, M. C., Stevens, B., Savic-Jovicic, V., Bretherton, C. S., Chlond, A., et al. (2009). Large-eddy simulations of a drizzling, stratocumulus-topped marine boundary layer. *Monthly Weather Review*, 137(3), 1083–1110. <https://doi.org/10.1175/2008MWR2582.1>
- Amante, C. (2009). ETOPO1 1 arc-minute global relief model: Procedures, data sources and analysis. NOAA Technical Memorandum NESDIS NGDC-24. National Geophysical Data Center, NOAA. <https://doi.org/10.7289/V5C8276M>
- Bailey, M. P., & Hallett, J. (2009). A comprehensive habit diagram for atmospheric ice crystals: Confirmation from the laboratory, air ii, and other field studies. *Journal of the Atmospheric Sciences*, 66(9), 2888–2899. <https://doi.org/10.1175/2009JAS2883.1>

### Acknowledgments

AWARE is supported by the DOE ARM Climate Research Facility and NSF Division of Polar Programs. The data used in this study (including the HSRL LCBH data product) are available in the ARM data archive (<http://www.archive.arm.gov>). Ten-second resolution HSRL data can be obtained from the University of Wisconsin-Madison HSRL Lidar Group (<http://lidar.ssec.wisc.edu>). ERA5 and ERA-Interim reanalysis data are accessible via the Copernicus Climate Change Service (C3S) Climate Data Store (CDS; <https://cds.climate.copernicus.eu>) and the ECMWF database (<https://apps.ecmwf.int/datasets/data/interim-full-daily/>), respectively. CERES and CALIOP observational data can be downloaded from the NASA Langley Research Center website ([https://ceres.larc.nasa.gov/order\\_data.php](https://ceres.larc.nasa.gov/order_data.php)) and the NASA Atmospheric Science Data Center website ([https://eosweb.larc.nasa.gov/project/calipso/calipso\\_table](https://eosweb.larc.nasa.gov/project/calipso/calipso_table)), respectively. AMPS data can be requested from the Ohio State University Polar Meteorology Group (<http://polarmet.osu.edu/AMPS/>). Wavelet software was provided by C. Torrence and G. Compo and is available at <http://paos.colorado.edu/research/wavelets/>. The authors wish to thank Paul Demott for the fruitful discussion. I.S. and J.V. are supported by the National Science Foundation grant PLR-1443495 and by the DOE grant DE-SC0017981. I.S. is also supported by DOE grant DE-SC0018046. A.F. and A. A. are supported by the NASA Radiation Science and Modeling, Analysis and Prediction programs. D.H. B. and S.H.W. are supported by National Science Foundation grant PLR-1443443 and by DOE grant DE-SC0017981. Contribution 1589 of Byrd Polar & Climate Research Center.

- Belosi, F., Santachiara, G., & Prodi, F. (2014). Ice-forming nuclei in Antarctica: New and past measurements. *Atmospheric Research*, 145–146, 105–111. <https://doi.org/https://doi.org/10.1016/j.atmosres.2014.03.030>
- Bromwich, D. H., Nicolas, J. P., Hines, K. M., Kay, J. E., Key, E. L., Lazzara, M. A., et al. (2012). Tropospheric clouds in Antarctica. *Reviews of Geophysics*, 50, RG1004. <https://doi.org/10.1029/2011RG000363>
- Carey, L. D., & Rutledge, S. A. (2000). The relationship between precipitation and lightning in tropical island convection: A C-band polarimetric radar study. *Monthly Weather Review*, 128(8), 2687–2710. [https://doi.org/10.1175/1520-0493\(2000\)128<2687:TRBPAL>2.0.CO;2](https://doi.org/10.1175/1520-0493(2000)128<2687:TRBPAL>2.0.CO;2)
- Chen, Y.-S., Verlinde, J., Clothiaux, E. E., Ackerman, A. S., Fridlind, A. M., Chamecki, M., et al. (2018). On the forward modeling of radar Doppler spectrum width from LES: Implications for model evaluation. *Journal of Geophysical Research: Atmospheres*, 123, 7444–7461. <https://doi.org/10.1029/2017JD028104>
- Clough, S. A., Kneizys, F. X., & Davies, R. W. (1989). Line shape and the water vapor continuum. *Atmospheric Research*, 23(3), 229–241. [https://doi.org/https://doi.org/10.1016/0169-8095\(89\)90020-3](https://doi.org/https://doi.org/10.1016/0169-8095(89)90020-3)
- Cober, S. G., & Isaac, G. A. (2012). Characterization of aircraft icing environments with supercooled large drops for application to commercial aircraft certification. *Journal of Applied Meteorology and Climatology*, 51(2), 265–284. <https://doi.org/10.1175/JAMC-D-11-022.1>
- Cober, S. G., Isaac, G. A., & Strapp, J. W. (2001). Characterizations of aircraft icing environments that include supercooled large drops. *Journal of Applied Meteorology*, 40(11), 1984–2002. [https://doi.org/10.1175/1520-0450\(2001\)040<1984:COAIET>2.0.CO;2](https://doi.org/10.1175/1520-0450(2001)040<1984:COAIET>2.0.CO;2)
- Cober, S. G., Strapp, J. W., & Isaac, G. A. (1996). An example of supercooled drizzle drops formed through a collision-coalescence process. *Journal of Applied Meteorology*, 35(12), 2250–2260. [https://doi.org/10.1175/1520-0450\(1996\)035<2250:AEOSDD>2.0.CO;2](https://doi.org/10.1175/1520-0450(1996)035<2250:AEOSDD>2.0.CO;2)
- Comiso, J. C. (2000). Variability and trends in Antarctic surface temperatures from in situ and satellite infrared measurements. *Journal of Climate*, 13(10), 1674–1696. [https://doi.org/10.1175/1520-0442\(2000\)013<1674:VATIAS>2.0.CO;2](https://doi.org/10.1175/1520-0442(2000)013<1674:VATIAS>2.0.CO;2)
- Comstock, K. K., Wood, R., Yuter, S. E., & Bretherton, C. S. (2004). Reflectivity and rain rate in and below drizzling stratocumulus. *Quarterly Journal of the Royal Meteorological Society*, 130(603), 2891–2918. <https://doi.org/10.1256/qj.03.187>
- Dee, D. P., Uppala, S. M., Simmons, A. J., Berrisford, P., Poli, P., Kobayashi, S., et al. (2011). The ERA-Interim reanalysis: Configuration and performance of the data assimilation system. *Quarterly Journal of the Royal Meteorological Society*, 137(656), 553–597. <https://doi.org/10.1002/qj.828>
- DeMott, P. J., Hill, T. C., & McFarquhar, G. M. (2018). Measurements of Aerosols, Radiation, and Clouds over the Southern Ocean (MARCUS) ice nucleating particle measurements field campaign report. DOE/SC-ARM-18-031, DOE Office of Science, Office of Biological and Environmental Research. Retrieved from <https://www.osti.gov/servlets/purl/1489372>
- Doviak, R. J., & Zrnić, D. S. (1993). Doppler spectra of weather signals. In R. J. Doviak, W. O. Second, & E. Zrnić (Eds.), (pp. 87–121). San Diego: Academic Press. <https://doi.org/https://doi.org/10.1016/B978-0-12-221422-6.50010-3>
- Eloranta, E. W. (2005). High spectral resolution lidar. In *Lidar: Range-resolved optical remote sensing of the atmosphere*, (pp. 143–163). New York, NY: Springer New York.
- Field, P. R., Heymsfield, A. J., Shipway, B. J., DeMott, P. J., Pratt, K. A., Rogers, D. C., et al. (2012). Ice in clouds experiment–layer clouds. Part II: Testing characteristics of heterogeneous ice formation in lee wave clouds. *Journal of the Atmospheric Sciences*, 69(3), 1066–1079. <https://doi.org/10.1175/JAS-D-11-026.1>
- Fridlind, A. M., van Diedenhoven, B., Ackerman, A. S., Avramov, A., Mrowiec, A., Morrison, H., et al. (2012). A FIRE-ACE/SHEBA case study of mixed-phase arctic boundary layer clouds: Entrainment rate limitations on rapid primary ice nucleation processes. *Journal of the Atmospheric Sciences*, 69(1), 365–389. <https://doi.org/10.1175/JAS-D-11-052.1>
- Garrett, T. J., & Zhao, C. (2006). Increased Arctic cloud longwave emissivity associated with pollution from mid-latitudes. *Nature*, 440, 787. <https://doi.org/10.1038/nature04636>
- Geoffroy, O., Brenguier, J.-L., & Burnet, F. (2010). Parametric representation of the cloud droplet spectra for LES warm bulk microphysical schemes. *Atmospheric Chemistry and Physics*, 10(10), 4835–4848. <https://doi.org/10.5194/acp-10-4835-2010>
- Geresdi, I., Rasmussen, R., Grabowski, W., & Bernstein, B. (2005). Sensitivity of freezing drizzle formation in stably stratified clouds to ice processes. *Meteorology and Atmospheric Physics*, 88(1), 91–105. <https://doi.org/10.1007/s00703-003-0048-5>
- Gossard, E. E. (1988). Measuring drop-size distributions in clouds with a clear-air-sensing doppler radar. *Journal of Atmospheric and Oceanic Technology*, 5(5), 640–649. [https://doi.org/10.1175/1520-0426\(1988\)005<0640:MDSDIC>2.0.CO;2](https://doi.org/10.1175/1520-0426(1988)005<0640:MDSDIC>2.0.CO;2)
- Gras, J. L. (1995). CN, CCN and particle size in Southern Ocean air at Cape Grim. *Atmospheric Research*, 35(2), 233–251. [https://doi.org/https://doi.org/10.1016/0169-8095\(94\)00021-5](https://doi.org/https://doi.org/10.1016/0169-8095(94)00021-5)
- Gras, J. L., & Keywood, M. (2017). Cloud condensation nuclei over the Southern Ocean: wind dependence and seasonal cycles. *Atmospheric Chemistry and Physics*, 17(7), 4419–4432. <https://doi.org/10.5194/acp-17-4419-2017>
- Hersbach, H., & Dee, D. (2016). ERA5 reanalysis is in production. *ECMWF Newsletter*, 147(7). <https://www.ecmwf.int/en/newsletter/147/news/era5-reanalysis-production>
- Heymsfield, A. J., Protat, A., Bouniol, D., Austin, R. T., Hogan, R. J., Delanoë, J., et al. (2008). Testing IWC retrieval methods using radar and ancillary measurements with in situ data. *Journal of Applied Meteorology and Climatology*, 47(1), 135–163. <https://doi.org/10.1175/2007JAMC1606.1>
- Hobbs, P. V., & Rangno, A. L. (1998). Microstructures of low and middle-level clouds over the Beaufort Sea. *Quarterly Journal of the Royal Meteorological Society*, 124(550), 2035–2071. <https://doi.org/10.1002/qj.49712455012>
- Hogan, R. J., Mittermaier, M. P., & Illingworth, A. J. (2006). The retrieval of ice water content from radar reflectivity factor and temperature and its use in evaluating a mesoscale model. *Journal of Applied Meteorology and Climatology*, 45(2), 301–317. <https://doi.org/10.1175/JAM2340.1>
- Holdridge, D., Ritsche, M., Prell, J., & Coulter, R. (2011). Balloon-Borne Sounding System (SONDE) handbook. ARM-TR-029, DOE Office of Science, Office of Biological and Environmental Research.
- Ikeda, K., Rasmussen, R. M., Hall, W. D., & Thompson, G. (2007). Observations of freezing drizzle in extratropical cyclonic storms during IMPROVE-2. *Journal of the Atmospheric Sciences*, 64(9), 3016–3043. <https://doi.org/10.1175/JAS3999.1>
- Jensen, A. A., & Harrington, J. Y. (2015). Modeling ice crystal aspect ratio evolution during riming: A single-particle growth model. *Journal of the Atmospheric Sciences*, 72(7), 2569–2590. <https://doi.org/10.1175/JAS-D-14-0297.1>
- Kirkpatrick, M. P., Ackerman, A. S., Stevens, D. E., & Mansour, N. N. (2006). On the application of the dynamic Smagorinsky model to large-eddy simulations of the cloud-topped atmospheric boundary layer. *Journal of the Atmospheric Sciences*, 63(2), 526–546. <https://doi.org/10.1175/JAS3651.1>
- Korolev, A. V., Isaac, G., Strapp, J., & Cober, S. (2002). Observation of drizzle at temperatures below -20 C. In *40th AIAA Aerospace Sciences Meeting & Exhibit* (p. AIAA-2002-0678).



- Lamb, D., & Verlinde, J. (2011). *Physics and chemistry of clouds*. New York, NY: Cambridge University Press.
- Lawson, R. P., Baker, B. A., Schmitt, C. G., & Jensen, T. L. (2001). An overview of microphysical properties of Arctic clouds observed in May and July 1998 during FIRE ACE. *Journal of Geophysical Research*, 106(D14), 14,989–15,014. <https://doi.org/10.1029/2000JD900789>
- Liu, J., Dedrick, J., Russell, L. M., Senum, G. I., Uin, J., Kuang, C., et al. (2018). High summertime aerosol organic functional group concentrations from marine and seabird sources at Ross Island, Antarctica, during AWARE. *Atmospheric Chemistry and Physics*, 18(12), 8571–8587. <https://doi.org/10.5194/acp-18-8571-2018>
- Lubin, D., Bromwich, D. H., Russell, L. M., Verlinde, J., & Vogelmann, A. M. (2015). ARM West Antarctic Radiation Experiment (AWARE) science plan. DOE/SC-ARM-15-040, DOE Office of Science, Office of Biological and Environmental Research. Retrieved from <https://www.osti.gov/servlets/purl/1232663>
- Lubin, D., & Vogelmann, A. M. (2006). A climatologically significant aerosol longwave indirect effect in the Arctic. *Nature*, 439, 453. <https://doi.org/10.1038/nature04449>
- Mather, J. H., & Voyles, J. W. (2013). The arm climate research facility: A review of structure and capabilities. *Bulletin of the American Meteorological Society*, 94(3), 377–392. <https://doi.org/10.1175/BAMS-D-11-00218.1>
- Mauritsen, T., Sedlar, J., Tjernström, M., Leck, C., Martin, M., Shupe, M., et al. (2011). An Arctic CCN-limited cloud-aerosol regime. *Atmospheric Chemistry and Physics*, 11(1), 165–173. <https://doi.org/10.5194/acp-11-165-2011>
- Meyers, M. P., DeMott, P. J., & Cotton, W. R. (1992). New primary ice-nucleation parameterizations in an explicit cloud model. *Journal of Applied Meteorology*, 31(7), 708–721. [https://doi.org/10.1175/1520-0450\(1992\)031<0708:NPINPI>2.0.CO;2](https://doi.org/10.1175/1520-0450(1992)031<0708:NPINPI>2.0.CO;2)
- Miles, N. L., & Verlinde, J. (2005). Observations of transient linear organization and nonlinear scale interactions in lake-effect clouds. Part I: Transient linear organization. *Monthly Weather Review*, 133(3), 677–691. <https://doi.org/10.1175/MWR-2879.1>
- Morris, V. R. (2006). Microwave radiometer (MWR) handbook. ARM-TR-016, DOE Office of Science, Office of Biological and Environmental Research.
- Morris, V. R. (2016). Ceilometer instrument handbook. DOE/SC-ARM-TR-020, DOE Office of Science, Office of Biological and Environmental Research.
- Morrison, H., & Grabowski, W. W. (2008). Modeling supersaturation and subgrid-scale mixing with two-moment bulk warm microphysics. *Journal of the Atmospheric Sciences*, 65(3), 792–812. <https://doi.org/10.1175/2007JAS2374.1>
- Morrison, H., Thompson, G., & Tatarskii, V. (2009). Impact of cloud microphysics on the development of trailing stratiform precipitation in a simulated squall line: Comparison of one- and two-moment schemes. *Monthly Weather Review*, 137(3), 991–1007. <https://doi.org/10.1175/2008MWR2556.1>
- Murphy, D. M., & Koop, T. (2005). Review of the vapour pressures of ice and supercooled water for atmospheric applications. *Quarterly Journal of the Royal Meteorological Society*, 131(608), 1539–1565. <https://doi.org/10.1256/qj.04.94>
- Ovchinnikov, M., Ackerman, A. S., Avramov, A., Cheng, A., Fan, J., Fridlind, A. M., et al. (2014). Intercomparison of large-eddy simulations of Arctic mixed-phase clouds: Importance of ice size distribution assumptions. *Journal of Advances in Modeling Earth Systems*, 6, 223–248. <https://doi.org/10.1002/2013MS000282>
- Parish, T. R., & Bromwich, D. H. (1991). Continental-scale simulation of the Antarctic katabatic wind regime. *Journal of Climate*, 4(2), 135–146. [https://doi.org/10.1175/1520-0442\(1991\)004<0135:CSSOTA>2.0.CO;2](https://doi.org/10.1175/1520-0442(1991)004<0135:CSSOTA>2.0.CO;2)
- Phillips, V. T. J., DeMott, P. J., & Andronache, C. (2008). An empirical parameterization of heterogeneous ice nucleation for multiple chemical species of aerosol. *Journal of the Atmospheric Sciences*, 65(9), 2757–2783. <https://doi.org/10.1175/2007JAS2546.1>
- Powers, J. G., Manning, K. W., Bromwich, D. H., Cassano, J. J., & Cayette, A. M. (2012). A decade of Antarctic science support through amps. *Bulletin of the American Meteorological Society*, 93(11), 1699–1712. <https://doi.org/10.1175/BAMS-D-11-00186.1>
- Pruppacher, H. R., & Beard, K. V. (1970). A wind tunnel investigation of the internal circulation and shape of water drops falling at terminal velocity in air. *Quarterly Journal of the Royal Meteorological Society*, 96(408), 247–256. <https://doi.org/10.1002/qj.49709640807>
- Pruppacher, H. R., & Klett, J. D. (1997). *Microphysics of clouds and precipitation*, (2nd ed.). Dordrecht, Netherlands: Kluwer Academic Publishers.
- Rambukkange, M. P., Verlinde, J., Eloranta, E. W., Flynn, C. J., & Clothiaux, E. E. (2011). Using Doppler spectra to separate hydrometeor populations and analyze ice precipitation in multilayered mixed-phase clouds. *IEEE Geoscience and Remote Sensing Letters*, 8(1), 108–112. <https://doi.org/10.1109/LGRS.2010.2052781>
- Randall, D. A. (1984). Stratocumulus cloud deepening through entrainment. *Tellus A: Dynamic Meteorology and Oceanography*, 36(5), 446–457. <https://doi.org/10.3402/tellusa.v36i5.11646>
- Rasmussen, R. M., Geresdi, I., Thompson, G., Manning, K., & Karplus, E. (2002). Freezing drizzle formation in stably stratified layer clouds: The role of radiative cooling of cloud droplets, cloud condensation nuclei, and ice initiation. *Journal of the Atmospheric Sciences*, 59(4), 837–860. [https://doi.org/10.1175/1520-0469\(2002\)059<0837:FDFISS>2.0.CO;2](https://doi.org/10.1175/1520-0469(2002)059<0837:FDFISS>2.0.CO;2)
- Rosenfeld, D., Chemke, R., DeMott, P., Sullivan, R. C., Rasmussen, R., McDonough, F., et al. (2013). The common occurrence of highly supercooled drizzle and rain near the coastal regions of the western United States. *Journal of Geophysical Research: Atmospheres*, 118, 9819–9833. <https://doi.org/10.1002/jgrd.50529>
- Schmale, J., Baccarini, A., Thurnherr, I., Henning, S., Efraim, A., Regayre, L., et al. (2019). Overview of the Antarctic Circumnavigation Expedition: Study of Preindustrial-like Aerosols and Their Climate Effects (ACE-SPACE). *Bulletin of the American Meteorological Society*. <https://doi.org/10.1175/BAMS-D-18-0187.1>
- Shaw, G. E. (1988). Antarctic aerosols: A review. *Reviews of Geophysics*, 26(1), 89–112. <https://doi.org/10.1029/RG026i001p00089>
- Shupe, M. D., Kollias, P., Poellot, M., & Eloranta, E. (2008). On deriving vertical air motions from cloud radar Doppler spectra. *Journal of Atmospheric and Oceanic Technology*, 25(4), 547–557. <https://doi.org/10.1175/2007JTECHA1007.1>
- Silber, I., Verlinde, J., Eloranta, E. W., & Cadetdu, M. (2018). Antarctic cloud macrophysical, thermodynamic phase, and atmospheric inversion coupling properties at McMurdo Station. Part I: Principal data processing and climatology. *Journal of Geophysical Research: Atmospheres*, 123, 6099–6121. <https://doi.org/10.1029/2018JD028279>
- Silber, I., Verlinde, J., Eloranta, E. W., Flynn, C. J., & Flynn, D. M. (2018a). HSRL Liquid cloud base height/MPL Liquid cloud base height. United States. <https://doi.org/10.5439/1438194>
- Silber, I., Verlinde, J., Eloranta, E. W., Flynn, C. J., & Flynn, D. M. (2018b). Polar liquid cloud base detection algorithms for high spectral resolution or micropulse lidar data. *Journal of Geophysical Research: Atmospheres*, 123, 4310–4322. <https://doi.org/10.1029/2017JD027840>
- Silber, I., Verlinde, J., Wang, S.-H., Bromwich, D. H., Fridlind, A. M., Cadetdu, M., & Eloranta, E. W. (2019). Cloud influence on ERA5 and AMPS surface downwelling longwave radiation biases in West Antarctica. *Journal of Climate*. <https://doi.org/10.1175/JCLI-D-19-0149.1>

- Simpfendorfer, L. F., Verlinde, J., Harrington, J. Y., Shupe, M. D., Chen, Y.-S., Clothiaux, E. E., & Golaz, J.-C. (2019). Formation of Arctic stratocumuli through atmospheric radiative cooling. *Journal of Geophysical Research: Atmospheres*. <https://doi.org/10.1029/2018JD030189>
- Stein, A. F., Draxler, R. R., Rolph, G. D., Stunder, B. J. B., Cohen, M. D., & Ngan, F. (2015). NOAA's HYSPLIT atmospheric transport and dispersion modeling system. *Bulletin of the American Meteorological Society*, 96(12), 2059–2077. <https://doi.org/10.1175/BAMS-D-14-00110.1>
- Stevens, D. E., Ackerman, A. S., & Bretherton, C. S. (2002). Effects of domain size and numerical resolution on the simulation of shallow cumulus convection. *Journal of the Atmospheric Sciences*, 59(23), 3285–3301. [https://doi.org/10.1175/1520-0469\(2002\)059<3285:EODSAN>2.0.CO;2](https://doi.org/10.1175/1520-0469(2002)059<3285:EODSAN>2.0.CO;2)
- Toon, O. B., & Ackerman, T. P. (1981). Algorithms for the calculation of scattering by stratified spheres. *Applied Optics*, 20(20), 3657–3660. <https://doi.org/10.1364/AO.20.003657>
- Toon, O. B., McKay, C. P., Ackerman, T. P., & Santhanam, K. (1989). Rapid calculation of radiative heating rates and photodissociation rates in inhomogeneous multiple scattering atmospheres. *Journal of Geophysical Research*, 94(D13), 16,287–16,301. <https://doi.org/10.1029/JD094iD13p16287>
- Torrence, C., & Compo, G. P. (1998). A practical guide to wavelet analysis. *Bulletin of the American Meteorological Society*, 79(1), 61–78. [https://doi.org/10.1175/1520-0477\(1998\)079<0061:APGTWA>2.0.CO;2](https://doi.org/10.1175/1520-0477(1998)079<0061:APGTWA>2.0.CO;2)
- Uin, J. (2016). Cloud condensation nuclei particle counter instrument handbook. DOE/SC-ARM-TR-168, DOE Office of Science, Office of Biological and Environmental Research.
- van den Broeke, M. R., & van Lipzig, N. P. M. (2003). Factors controlling the near-surface wind field in Antarctica. *Monthly Weather Review*, 131(4), 733–743. [https://doi.org/10.1175/1520-0493\(2003\)131<0733:FCTNSW>2.0.CO;2](https://doi.org/10.1175/1520-0493(2003)131<0733:FCTNSW>2.0.CO;2)
- van Diedenhoven, B., Fridlind, A. M., & Ackerman, A. S. (2011). Influence of humidified aerosol on lidar depolarization measurements below ice-precipitating Arctic stratus. *Journal of Applied Meteorology and Climatology*, 50(10), 2184–2192. <https://doi.org/10.1175/JAMC-D-11-037.1>
- van Diedenhoven, B., Fridlind, A. M., Ackerman, A. S., & Cairns, B. (2012). Evaluation of hydrometeor phase and ice properties in cloud-resolving model simulations of tropical deep convection using radiance and polarization measurements. *Journal of the Atmospheric Sciences*, 69(11), 3290–3314. <https://doi.org/10.1175/JAS-D-11-0314.1>
- Verlinde, J., Rambukkange, M. P., Clothiaux, E. E., McFarquhar, G. M., & Eloranta, E. W. (2013). Arctic multilayered, mixed-phase cloud processes revealed in millimeter-wave cloud radar Doppler spectra. *Journal of Geophysical Research: Atmospheres*, 118, 13,199–13,213. <https://doi.org/10.1002/2013JD020183>
- Vogelmann, A. M., Fridlind, A. M., Toto, T., Endo, S., Lin, W., Wang, J., et al. (2015). RACORO continental boundary layer cloud investigations: 1. Case study development and ensemble large-scale forcings. *Journal of Geophysical Research: Atmospheres*, 120, 5962–5992. <https://doi.org/10.1002/2014JD022713>
- Wielicki, B. A., Barkstrom, B. R., Harrison, E. F., Lee, R. B., Smith, G. L., & Cooper, J. E. (1996). Clouds and the Earth's Radiant Energy System (CERES): An Earth Observing System Experiment. *Bulletin of the American Meteorological Society*, 77(5), 853–868. [https://doi.org/10.1175/1520-0477\(1996\)077<0853:CATERE>2.0.CO;2](https://doi.org/10.1175/1520-0477(1996)077<0853:CATERE>2.0.CO;2)
- Winker, D. M., Pelon, J. R., & McCormick, M. P. (2003). The CALIPSO mission: spaceborne lidar for observation of aerosols and clouds (Vol. 4893, pp. 1–11). Retrieved from <https://doi.org/10.1117/12.466539>
- Witze, A. (2016). Antarctic clouds studied for first time in five decades. *Nature*, 529(7584), 12.
- Zhang, D., Wang, Z., & Liu, D. (2010). A global view of midlevel liquid-layer topped stratiform cloud distribution and phase partition from CALIPSO and CloudSat measurements. *Journal of Geophysical Research*, 115, D00H13. <https://doi.org/10.1029/2009JD012143>
- Zipser, E. J., & Lutz, K. R. (1994). The vertical profile of radar reflectivity of convective cells: A Strong indicator of storm intensity and lightning probability? *Monthly Weather Review*, 122(8), 1751–1759. [https://doi.org/10.1175/1520-0493\(1994\)122<1751:TVPORR>2.0.CO;2](https://doi.org/10.1175/1520-0493(1994)122<1751:TVPORR>2.0.CO;2)